CrystEngComm

ROYAL SOCIETY OF CHEMISTRY

PAPER

View Article Online
View Journal | View Issue

Cite this: *CrystEngComm*, 2022, **24**, 5630

Exploring halogen···halogen interactions in supramolecular self-assemblies of BODIPY networks†

Burcu Topaloğlu Aksoy, Burcu Dedeoglu, Yunus Zorlu, Mehmet Menaf Ayhan * and Bünyemin Çoşut *

Received 6th June 2022,
Accepted 11th July 2022

DOI: 10.1039/d2ce00776b

rsc.li/crystengcomm

In this study, the efficiency of halogen···halogen interactions to control supramolecular assemblies of boron dipyrromethene (BODIPY) (**B1**–**B5**) derivatives was explored. BODIPY scaffolds were systematically decorated with iodine groups to promote halogen···halogen interactions. Single crystal X-ray diffraction analysis revealed the formation of XB interactions, I···I and I···F contacts, which led to impressive halogen-bonded supramolecular tubular-like (**B1**), domino-like (**B2**), 1D linear chain (**B3**), helical (**B4**), and 1D linear chain (**B5**) self-assemblies. The molecular electrostatic potential (MEP) showed the presence of σ holes on the outer tip of the iodine groups for all compounds and the positive potential increases with each additional iodine substitution on the BODIPY scaffold. Symmetry-adapted perturbation theory (SAPT) analysis showed that the dispersion and electrostatic components are the major source for all XB formations. The additional AIM theory analysis showed the bond critical points (BCPs) between I···I, F confirming the formation of halogen bonds in these assemblies.

Introduction

Noncovalent interactions, such as hydrogen bonding (HB), halogen bonding (XB), electrostatic, dipole–dipole and van der Waals interactions, represent an essential set of tools for the building of supramolecular architectures with precisely controlled structures and functions.[1–6] Thanks to the dynamic and reversible properties of noncovalent interactions, supramolecular assemblies have been used in widespread applications such as catalysis,[7–10] solar cells,[11–13] crystal engineering,[14,15] sensors,[16,17] and stimuli-responsive and self-healing materials.[18–23]

Among these interactions, XB has become increasingly attractive as a routine and predictable tool in supramolecular chemistry, due to its highly directional nature, significant strength, and tunable length.[24–32] XB is a net attractive interaction between an electrophilic region of a halogen atom (I, Br, Cl, F) in an acceptor molecule (Lewis acid, halogen bonding donor) and a nucleophilic region (N, O, S, P, I, Br, Cl) of another molecule (Lewis base, halogen bonding acceptor). Due to the anisotropic distribution of its electron density, a halogen atom can act as a nucleophile at the equator and as an electrophile along the pole direction at the same time which can lead to halogen···halogen (X2 synthons) interaction. The nature and strength of halogen···halogen interactions strongly depend on their geometry and they are generally classified as either type-I or type-II (Scheme 1a–c).[33,34] The type-I is a geometry-based interaction that results from close packing and is common for all halogens (I, Br, Cl, F), whereas type-II results from an electrophile–nucleophile pairing contact stabilized by electrostatic forces, and only type-II interactions are considered to be true XB. However, recent studies have shown that despite the generally accepted rules, halogen bonding can exist between two similarly charged halogen atomic sites (type-III, Scheme 1d).[35–38] Thus, with the addition of type-III interactions into the XB toolbox, halogen bonding can be further pushed to the design and creation of excellent supramolecular networks.[39–45]

In this context, the design and control of the self-assembly of functional materials is highly desirable to be able to govern the resulting electronic, optical, and mechanical properties for chosen applications. BODIPY derivatives are one of the functional materials much needed and it is highly desirable to control their self-assembly, yet they have been comparatively less explored, due to challenges of the precise design and control of the noncovalent interactions in their complex structure.[46–53]

BODIPY scaffolds can be easily functionalized at several sites to construct ordered materials with predetermined

Department of Chemistry, Gebze Technical University, Gebze, Kocaeli, 41400, Türkiye. E-mail: menafayhan@gtu.edu.tr, bcosut@gtu.edu.tr

† Electronic supplementary information (ESI) available: Experimental details, crystal data parameters, and additional figures. CCDC 2108982 for **B1**, 2108984 for **B2**, 2108981 for **B3**, 2108983 for **B4**, and 2108985 for **B5** contain the supplementary crystallographic data for this paper. For ESI and crystallographic data in CIF or other electronic format see DOI: https://doi.org/10.1039/d2ce00776b

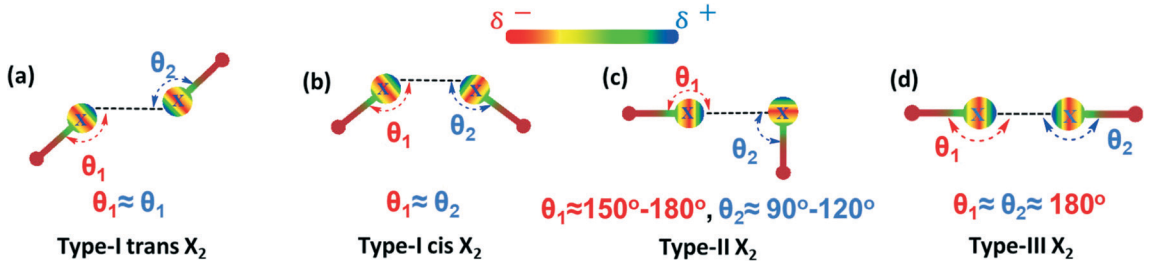

Scheme 1 Schematic representation of the halogen···halogen interactions (X = halogen atom) in dimeric synthons.

structures and properties, which are used in widespread applications in fields such as fluorescence imaging and sensing, dye sensitized solar cells, photocatalysis, singlet oxygen generation and photodynamic therapy.[54–59]

Recently, others and we have demonstrated the self-assembly of various BODIPY derivatives through diverse methodologies.[60–67] As these studies revealed, particularly, XB interactions are a useful tool to modulate the supramolecular assembly and the resulting electronic, optical, and mechanical properties of BODIPYs. Herein, as a follow-up study, the present work demonstrates further efforts to utilize halogen···halogen interactions in our crystal engineering efforts to construct new BODIPY supramolecular assemblies.

To this end, we have designed and synthesized a series of systematically varied iodine incorporated BODIPYs (**B1–B5**) with the aim of invoking multiple halogen···halogen interaction formations (Scheme 1 and S1†). In this systematic study, we attempt to evaluate the scaffold effects on halogen bonding strength and differences in their resulting crystal structures (Scheme 2).

1. Experimental section

1.1. General methods

All chemicals and solvents were purchased from Sigma Aldrich and TCI Chemicals and used as supplied without further purification unless stated otherwise. Full details of the synthetic and characterization data of **B1–B5** are described in the ESI.†

1.2. X-ray crystallography

Single crystal X-ray diffraction data for BODIPY derivatives (**B1–B5**) were obtained with a Bruker APEX II QUAZAR three-circle diffractometer. Indexing was performed using APEX2.[68] Data indexing, integration and reduction were carried out with Bruker SAINT.[69] Absorption correction was performed by the multi-scan method implemented in Bruker SADABS.[70] Crystal structures were solved using SHELXT and then refined by full-matrix least-squares refinements on F^2 using SHELXL in the Olex2 software package.[71,72] The positions of all hydrogen atoms which were bonded to carbon were geometrically optimized with the following HFIX instructions in SHELXL: HFIX 137 for the $-CH_3$, HFIX 23 for the $-CH_2$, and HFIX 43 for the CH of the aromatic rings. Finally, their displacement parameters were set to isotropic thermal displacement parameters (U_{iso}(H) = 1.2 × U_{eq} for $CH_{aromatic}$ and CH_2 and U_{iso}(H) = 1.5 × U_{eq} (CH_3 groups)). The crystal structures of **B1** and **B2** were a non-merohedral twin, showing a domain accounting for *ca.* 16%, and 47%, respectively. The twin data of these two structures were refined using an hklf-5 file. Crystal structure validations and geometrical calculations were performed using Platon software.[73] Mercury software was applied for the cif file visualization.[74] Additional crystallographic data with CCDC reference numbers of the BODIPY derivatives (2108982 for **B1**, 2108984 for **B2**, 2108981 for **B3**, 2108983 for **B4**, and 2108985 for **B5**) have been deposited within the Cambridge Crystallographic Data Center.

1.3. Computational methodology

Molecular electrostatic potential surfaces were calculated with the density functional M06-2X as implemented in Gaussian 16.[75] For iodine, DGDZVP and for the rest of the atoms, the 6-311+G(d,p) basis sets were used. "Atom in molecules" (AIM) analysis was performed to analyze the

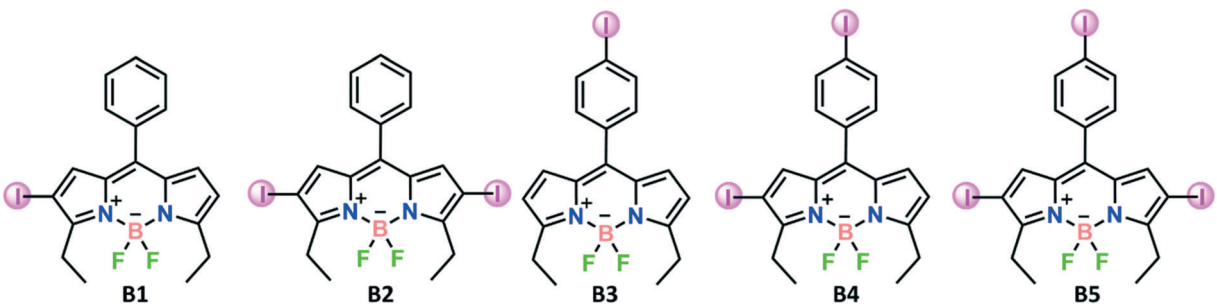

Scheme 2 Chemical structure of **B1–B5**.

topological critical points with Multiwfn software (v. 3.3.5),[76] using the wave functions generated by Gaussian 16. The analysis of non-covalent interactions was carried out by employing the symmetry-adapted perturbation theory (SAPT) which separates out the components of a given interaction such as electrostatic (E_{elst}), exchange–repulsion (E_{exch}), induction (E_{ind}), and dispersion (E_{disp}).[77–79] To achieve this decomposition, the Hamiltonian is partitioned into monomeric Fock operators, Møller–Plesset fluctuation operators, and intermolecular interaction operators. All SAPT calculations were performed with the Psi4 program using density fitting at the sSAPT0/aug-cc-pVDZ level.[80]

2. Results and discussion

2.1. Analysis of photophysical properties

The photophysical properties of the synthesized iodine incorporated BODIPY derivatives (**B0–B5**) in solution at 2 × 10^{-6} M were investigated by UV-vis spectrophotometry (Fig. 1 and S19†). The maximum absorption peaks of compound **B0** at around 512 nm are attributed to the absorption of BODIPY cores and this absorption is due to transition from the S_0 to S_1 states. The incorporation of iodine atoms at the 2- and 6-positions (periphery) of the BODIPY scaffold is known to cause a significant red shift in the absorption spectrum, whereas an iodine atom on the *meso*-phenyl group of the BODIPY scaffold causes only a small red shift in the absorption spectrum.[59,81,82] As expected, the absorption bands are red shifted for all BODIPY derivatives (**B1–B5**) with addition of halogen atoms. The shift is much larger for the iodine derivatives on the periphery compared to that for those on the *meso*-phenyl group. The molar absorptivity coefficients of the compounds **B0–B5** at their maximum wavelengths were found as 1.60, 1.36, 0.94, 0.67, 0.64 and 1.54 (10^5 M^{-1} cm^1), respectively. All spectral data based on absorption measurements are summarized in Table S1.† We should note that we have measured the absorbance spectra of **B1–B5** at different concentrations and did not observe any changes in the corresponding absorbance spectra of **B1–B5** in solution, which suggests that there is no assembly in solution (Fig. S20†).

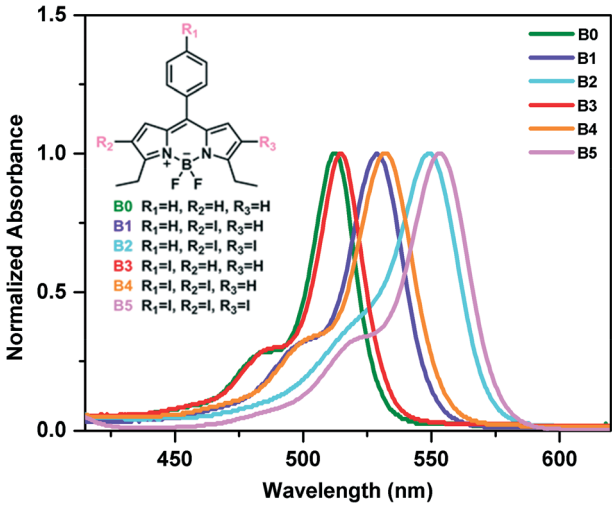

Fig. 1 Absorption spectra of synthesized compounds (**B0–B5**) in DCM.

2.2. Description of crystal structures

The BODIPY (**B1–B5**) crystals were investigated by single crystal X-ray diffraction analysis to gain deep insight into the spatial arrangement of the molecules, crystal packing, and intermolecular interactions. Crystallographic data and refinement details of the data collection are given in Tables S2–S5.† Clear red needle-like single crystals of BODIPYs **B1–B5** were obtained by slow evaporation of solvents from a dichloromethane/hexane (1 : 2) mixture at ambient temperature, which resulted in single crystals with the triclinic $P\bar{1}$ (**B1**), monoclinic $C2/c$ (**B2**), orthorhombic $C2221$ (**B3**), monoclinic $P2_1/c$ (**B4**), and orthorhombic $Pbcn$ (**B5**) space groups. The conjugated backbone of the BODIPY scaffold (C_9BN_2) exhibits a nearly planar molecular configuration with negligible interplanar twists for all structures (**B1–B5**) as shown in Fig. 2. The inter-ring dihedral angles between the *meso*-phenyl group and the BODIPY π-frame are 68.59° for **B1**, 60.50° for **B2**, 58.78° for **B3**, 61.57° for **B4** and 60.82° for **B5**, which match well with those of reported BODIPY derivatives lacking β-pyrrole substituents.[83–85]

The crystal packing structure (Fig. 3A) of **B1** displays both CH···F hydrogen bonding (C16–H16A···F2, $d_{(C16\cdots F2)}$ = 3.516 Å) and I···π_{BODIPY} interactions ($d_{(I\cdots BODIPY)}$ = 3.758 Å). These two cooperative interactions form a 1D domino-like arrangement (Fig. 3B) running along the *a*-axis with a slipping angle (θ) of 32.61°. The average vertical distance between parallel BODIPY aromatic frames (C_9BN_2) is 3.336 Å. Furthermore, this 1D arrangement leads to a tubular architecture (Fig. 3C) by a combination of I···π_{phenyl} interactions ($d_{(I\cdots phenyl)}$ = 3.698 Å) along the *a*-axis. The I···π_{phenyl} and I···π_{BODIPY} interactions are recognized as a red spot as shown in the Hirshfeld surface of **B1** mapped with d_{norm} and are identified with a ratio of 6.5% of I···π (I···C/C···I) interactions in the 2D fingerprint plot (Fig. 3D).

The domino-like arrangement with a slipping angle (θ) of 36.68° in the crystal packing (Fig. 4A and B) of **B2** was formed through the weak CH···F hydrogen bonding (C16–H16B···F1, $d_{(C16\cdots F1)}$ = 3.355 Å; C18–H18B···F2, $d_{(C18\cdots F2)}$ = 3.415 Å) and I···π_{BODIPY} interactions ($d_{(I\cdots BODIPY)}$, Fig. 4D = 3.764 Å). It is worth noting that although the I···I contacts ($d_{I1\cdots I2}$ = 3.976 Å and 4.043 Å, Fig. 4C) are slightly longer than the sum of van der Waals radii of two iodine atoms ($r_{vdW}(I) + r_{vdW}(I)$ = 3.96 Å), the Hirshfeld surface analysis of **B2** exhibits the proportion of the I···I contacts as 3% on the 2D fingerprint plot. Apparently, the four I···I XB interactions per BODIPY molecule seem highly directional to form a herringbone pattern in the crystal packing (Fig. 4A).

The crystal structure of **B3** displayed highly directional symmetrical bifurcated $-BF_2$···I XB contacts forming a 1D chain structure running along the *b*-axis (Fig. 5B). The I···F

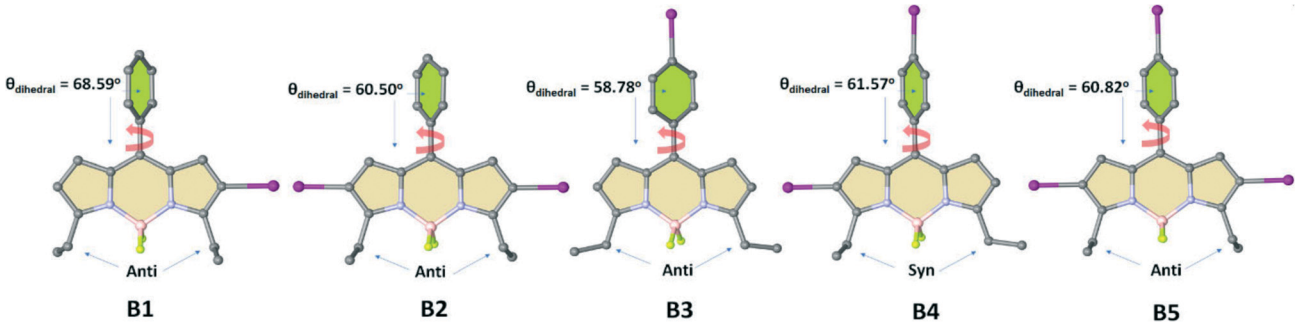

Fig. 2 Crystal structures of BODIPYs (**B1**–**B5**), illustrating the conjugated backbone (clear yellow) of BODIPY and the dihedral angles between aromatic rings (yellow rings). All hydrogen atoms were omitted for clarity.

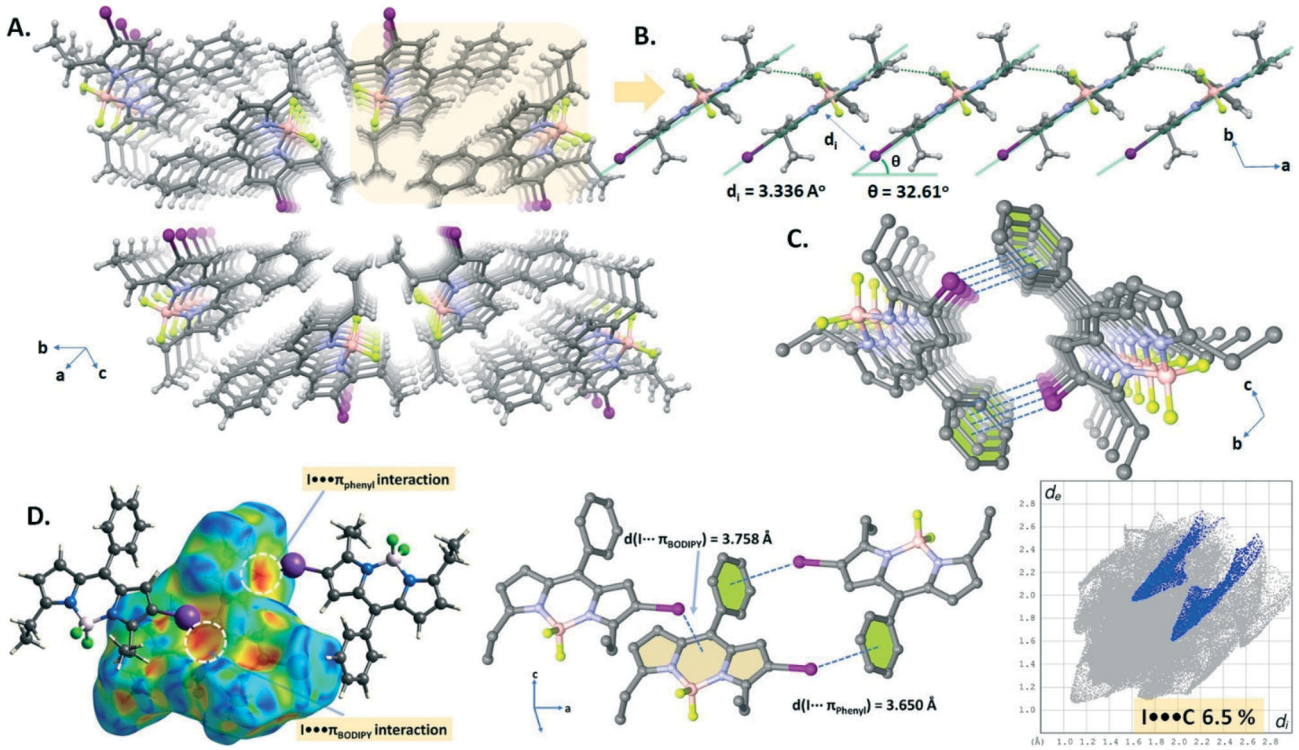

Fig. 3 (A) Perspective view of the crystal packing of **B1**. (B) Illustration of the 1D domino-like arrangement running along the *a*-axis. (C) Perspective view of the tubular-like architecture in the crystal packing of **B1** through the I···π_{phenyl} interactions. (D) Hirshfeld surface of **B1** mapped with d_{norm} and the 2D fingerprint plot representing the I···π_{phenyl} and I···π_{BODIPY} interactions.

contacts ($d_{(I1\cdots F1)}$ = 3.353(3) Å) are slightly shorter by 3% than the sum of van der Waals radii of two atoms (r_{vdW}(I) + r_{vdW}(F) = 3.45 Å (relative distance $R = d/\sum(I\cdots N)_{vdW}$ = 0.97 for I1···F1)) and comprise only 4.2% of the total surface area, appearing as a red spot as shown in the Hirshfeld surface mapped with d_{norm} (Fig. 5C). Interestingly, a sinusoidal wave-like pattern (along the *bc* plane, Fig. 5A) was formed through the weak CH···F hydrogen bonding interactions (C8–H8B···F1, $d_{(C8\cdots F1)}$ = 3.393 Å) and edge-to-face CH···π interactions (C7–H···π) between the 1D halogen bonded chain structures.

In the crystal structure of **B4**, the I···I halogen bond (I1–I2 = 3.7299(18) Å, $\sum(I\cdots I)_{vdW}$ = 3.96 Å, relative distance $R = d/\sum(I\cdots I)_{vdW}$ = 0.94) promotes the formation of right-handed (P) and left-handed (M) supramolecular halogen-bonded single helices along the *b*-axis, in which one turn completes with a *d* = 10.554 Å pitch distance (Fig. 6A–C). These P and M supramolecular helices are further connected by –BF_2···I XBs (I1–F1 = 3.221(4) Å, $\sum(I\cdots F)_{vdW}$ = 3.45 Å, relative distance $R = d/\sum(I\cdots F)_{vdW}$ = 0.93) to form a 2D supramolecular layered network of **B4** (Fig. 6D). The I···I and –BF_2···I XBs were illustrated in the *d*-norm mapped Hirshfeld surface, showing 1.9% and 2.5% of the total Hirshfeld surface (Fig. 6E and F).

The crystal structure of **B5** revealed that directional symmetrical bifurcated –BF_2···I XB contacts ($d_{(I1\cdots F1)}$ = 3.463(3) Å) afford a 1D linear chain (Fig. 7C) motif running along the *b*-axis, which was similar to that of **B3**. Moreover,

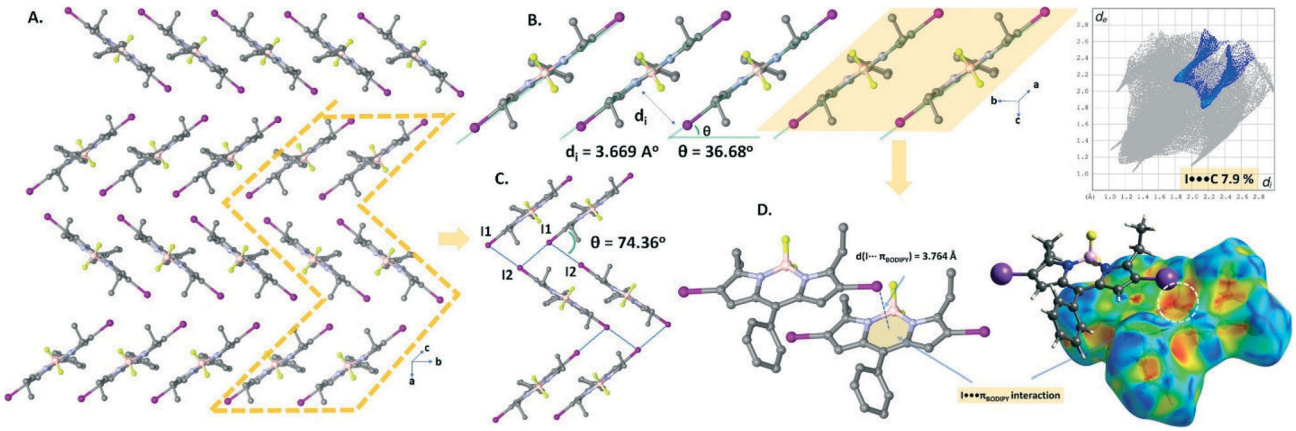

Fig. 4 (A) and (C) Perspective views of the herringbone-like arrangement in the crystal packing of **B2**. (B) Representation of the domino-like pattern running along the *b*-axis. (D) The shape-index surface of **B2** mapped with d_{norm} and the 2D fingerprint plot showing the I···π_{BODIPY} interactions.

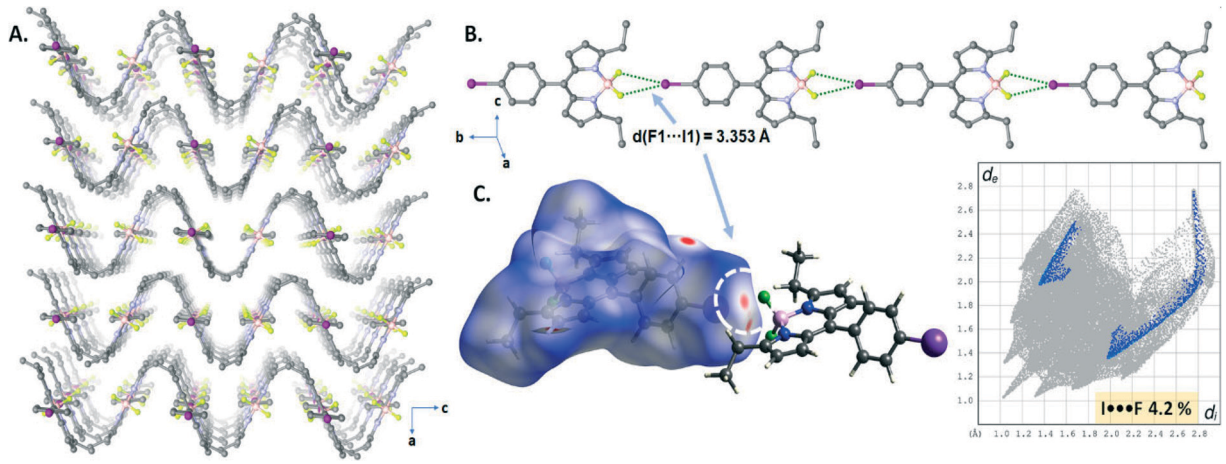

Fig. 5 (A) Perspective view of the sinusoidal wave-like pattern along the *ac* plane in **B3**. (B) View of the directional symmetrical bifurcated –BF_2···I XB contacts forming a 1D chain in the crystal packing. (C) Hirshfeld surface representation and the 2D fingerprint plot of symmetrical bifurcated I···F XBs.

the resulting 1D chains are expanded into a 3D supramolecular halogen-bonded framework (Fig. 7A) by the I···I halogen bond (I1–I2 = 3.8133(6) Å, $\sum(I\cdots I)_{vdW}$ = 3.96 Å, relative distance $R = d/\sum(I\cdots I)_{vdW}$ = 0.96). As depicted in Fig. 7E, the I···I and –BF_2···I XBs account for 3.8% and 3.7% of the total Hirshfeld surface (Fig. 7D) on the 2D fingerprint plots. Topologically, **B5** was analyzed to better understand the 3D architecture. As illustrated in Fig. 7B, it is a 3D framework with two-fold interpenetrated halogen bonding networks (class IIa, z = 2). The single framework, which has large pores with window dimensions of 9.38 Å × 8.28 Å (Fig. 7A), can be simplified as a uninodal 6-connected **pcu** network having the point symbol $4^{12}\cdot6^3$ (Fig. 3A).

Finally, we have also examined the intermolecular π-electron cloud interactions in the BODIPY assemblies. The short intermolecular $\pi_{BODIPY}\cdots\pi_{BODIPY}$ interactions (3.689(8) Å for **B1** and 3.732(8) Å for **B2**) between the pyrrole moieties of BODIPY make an important contribution to the stabilization of the crystal packing of **B1** and **B2** (see Fig. S27a and S29a†). It should be noted that the shape index and curvedness surfaces of **B1** and **B2** look quite similar because the molecules are arranged into similar domino-like stacks. The pattern of adjacent red and blue triangles that appear on the shape index surfaces of **B1** and **B2** clearly demonstrates the presence of short π–π interactions, which account for 3.3% and 4.2% of the total Hirshfeld surfaces, respectively (Fig. S27b and S29b†). The curvedness maps of both molecules exhibit a large flat region corresponding to the pyrrole rings, which also shows clearly π···π interactions. On the other hand, compounds **B3**, **B4** and **B5** do not show the close π–π stacking interactions because there is no evidence of the adjacent red and blue triangles when looking at the comparative shape index surface maps of all structures (Fig. S31†). In addition, **B3**–**B5** do not show a large flat region corresponding to the pyrrole rings. The closest CH···π interaction (C14–H14···π, d(H···π) = 2.826 Å for **B1**, C7–H7···π, d(H···π) = 2.95, see Fig. S28a and S30a†) is seen in **B1** and **B3**, as illustrated in the shape index-mapped Hirshfeld surfaces (Fig. S28b and S30b†). The CH···π interactions can be

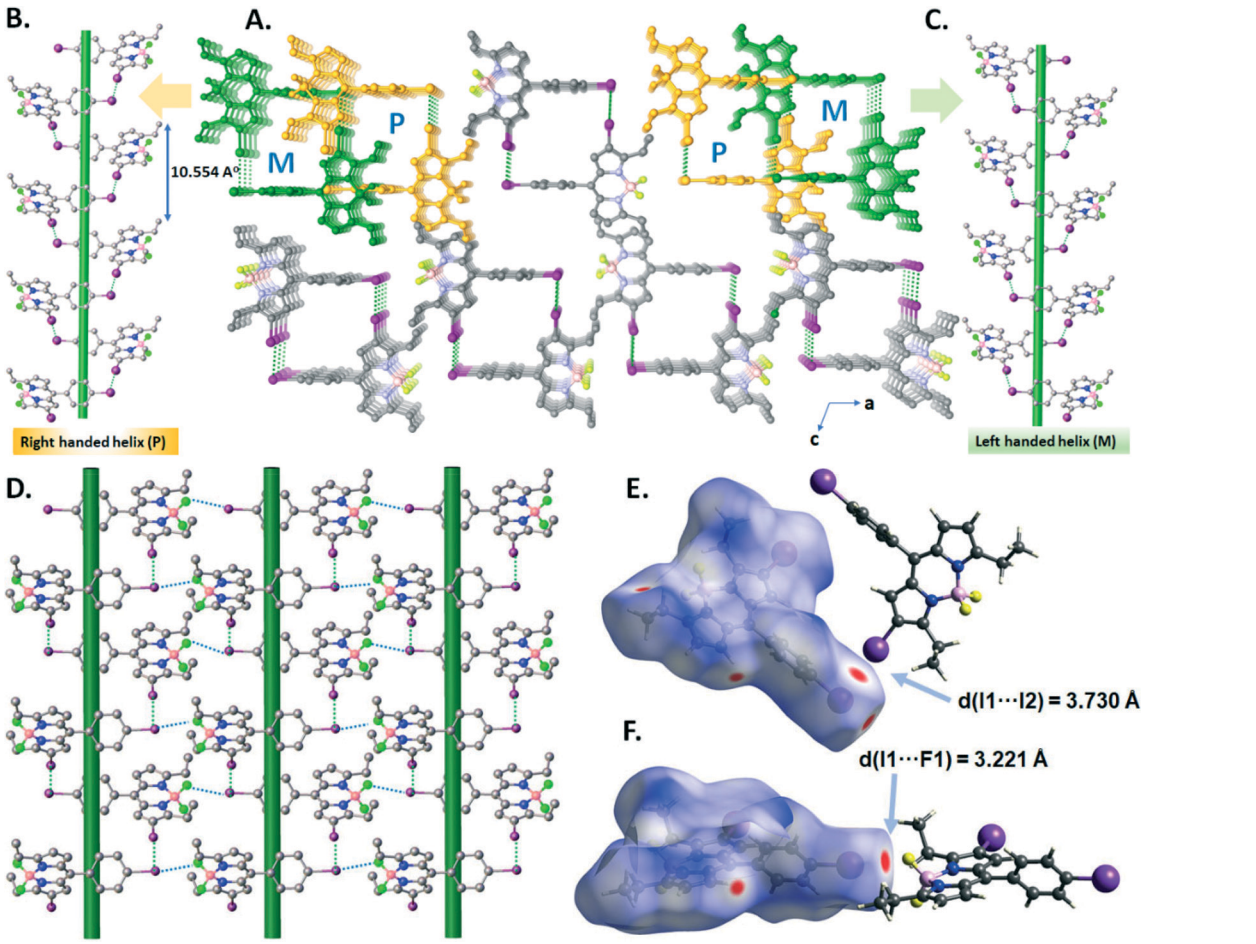

Fig. 6 (A) View of the 3D supramolecular network showing P and M helicity in the crystal packing in **B4**. (B) and (C) Illustrations of P and M helices. (D) A 2D halogen-bonded layer formed by I···F (blue dotted lines) and I···I (green dotted lines) XB interactions showing their *d*-norm mapped Hirshfeld surface representations (E and F).

viewed from a pair of typical "wings" at the top left and bottom right of the 2D plots (Fig. S22–S26†). The C···H/H···C contacts of **B1–B5** constitute 12.2%, 6%, 25.3%, 18.2%, and 16.3% of the total Hirshfeld surface attributing to the CH···π interactions.

2.3. Computational analyses

To examine whether the halogen···halogen interactions inducing supramolecular self-assembly of BODIPY networks are intrinsically stable or are merely a consequence of the crystal packing, we carried out extensive density functional theory calculations including molecular electrostatic potentials and HOMO–LUMO analysis for the monomers as the representative units of the networks of **B1–B5**. The interactions in these networks are also analyzed *via* the AIM and SAPT procedure in the dimers of the networks of **B1–B5**.

2.3.1. Molecular electrostatic potential. The molecular electrostatic potential (MEP) has been used to investigate and visualize the σ-hole formations of monomers **B1–B5** to understand the nature of XBs (Fig. 8). As expected, a negative potential appears on the fluoro atoms of BF_2, and a positive potential surrounding the aromatic rings of benzene and iodobenzene is clear. It is evident that a positive potential exists on the outer tip of the iodine confirming the σ-hole formation in all compounds. This positive potential is +16.0 kcal mol^{-1} in **B1** and increases to +20.7 and +21.4 in **B2** as the iodo substitution on the periphery of the BODIPY scaffold increases. On the other hand, the negative potential of BF_2 decreases from −33.3 (**B1**) to −31.7 (**B2**) kcal mol^{-1}. Indeed, this trend is observed in all series: higher iodo substitution, whether it is on the periphery or on the *meso*-phenyl, renders the iodo groups more positive and the BF_2 group less negative. When iodo is placed on the *meso*-phenyl, the positive potential increases from +16.0 (**B1** where iodo is on the periphery) to +20.6 kcal mol^{-1} in **B3**, and the positive value of the iodo on an aromatic group is even increased with iodo substitutions on the periphery. This positive potential increases to +21.3 and +22.3 in **B4** and **B5**, respectively. In **B4**, one iodo is on the *meso*-phenyl and one iodo is on the periphery. The positive potential of both iodo groups increases with respect to **B1** and **B3**: for the periphery from +16.0 to +19.7 and for the aromatic iodo from +20.6. to +21.3. When one more iodo is attached on the periphery in **B5**, the positive potential of the three iodo groups becomes almost

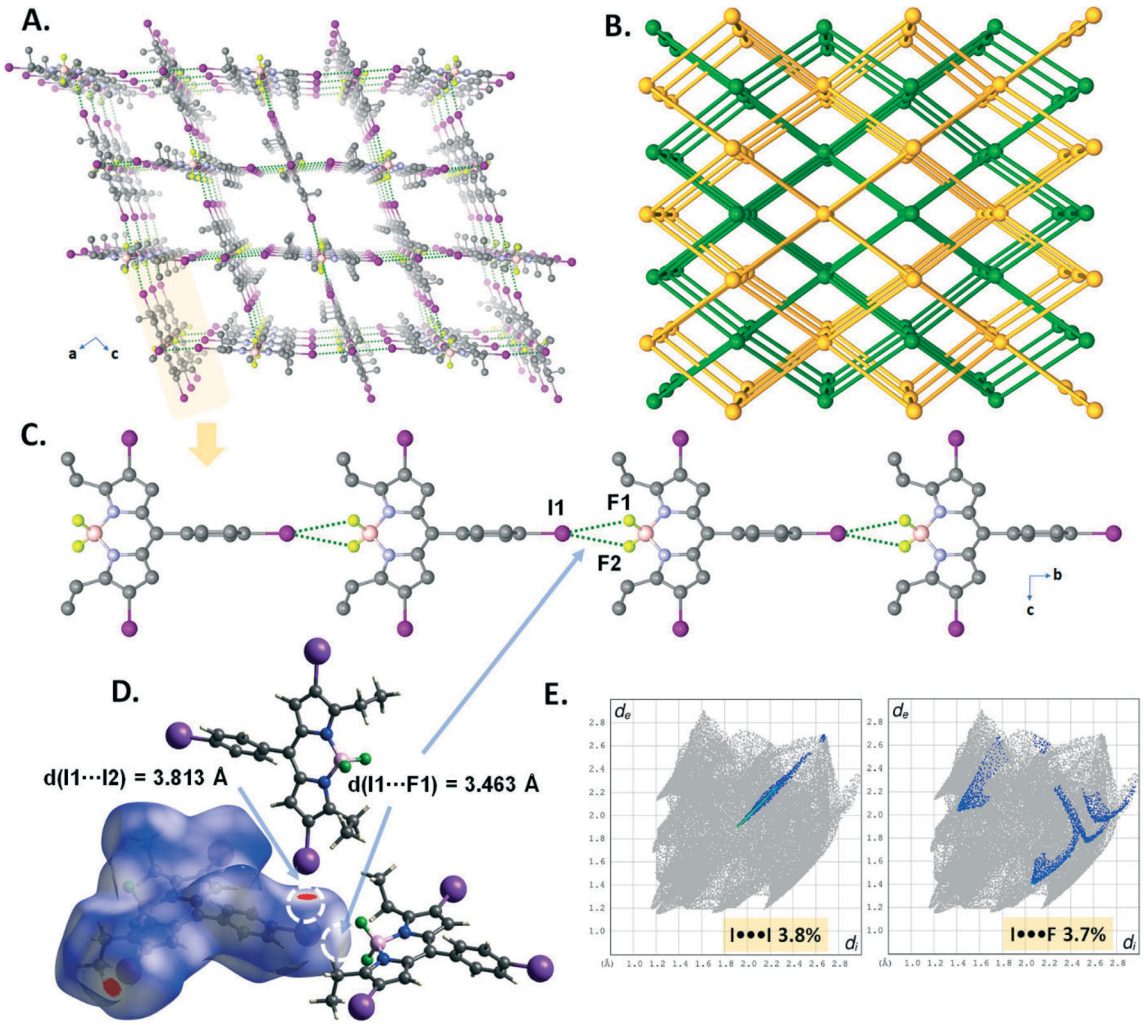

Fig. 7 (A) View of the 3D halogen-bonded framework showing a single network in the crystal packing in **B5**. (B) Illustration of two-fold halogen-bonded interpenetration formed through –BF_2···I and I···I contacts. (C) View of the directional symmetrical bifurcated –BF_2···I XB contacts forming a 1D chain in **B5**. (D) and (E) Hirshfeld surface representations of symmetrical bifurcated –BF_2···I and I···I XBs showing the 2D fingerprint plots.

equal and they have the most positive potential whereas a less negative potential is observed on BF_2 among all five structures.

Furthermore, the frontier molecular orbitals have been analyzed and the orbitals are depicted in Fig. S21.† The electron density of the highest occupied molecular orbital (HOMO) is distributed mostly over the BODIPY core for **B1–B5**. The electron density is shifted towards the periphery iodo for the lowest unoccupied molecular orbital (LUMO) but is almost completely localized on the BODIPY core. UV-vis and electrostatic potential map analyses also confirmed that iodo at *meso*-phenyl has a minimum effect on the electron density of BODIPY.

2.3.2. Analyses of electron density topology and interaction energies. The quantum theory of atoms in molecules (QTAIM) theory has been employed to reveal the nature of the interactions between the dimers of **B1–B5**. In AIM theory, interatomic interactions can be characterized with the topological parameters including the electron density (r), Laplacian ($\nabla^2\rho$) and energy density (H) at the bond critical points (BCPs). The magnitudes of electron density, Laplacian, and energy density at the intermolecular BCPs of interest are listed in Table S6.† The BCPs of all studied structures possess a positive Laplacian and energy density, indicating weak pure closed-shell interactions with a small electron density (Table S6†).

For the network of **B1**, two types of dimers have been considered: **B1-I** as the repike arrangement and **B1-II** as a unit of tubular like architecture (Fig. 9). In **B1-I**, there is a bond path connecting iodine and the BODIPY core indicating the presence of the I···π_{BODIPY} interaction. There are two F···H BCPs confirming the presence of CH···F hydrogen bonding interactions. In addition, there are other BCPs not included in Table S6† and these are associated with π–π interactions of the two BODIPY cores and other dispersion interactions. In **B1-II**, there are two types of intermolecular BCPs: first, the I···π_{phenyl} interaction and second, the CH···I hydrogen bonding interaction.

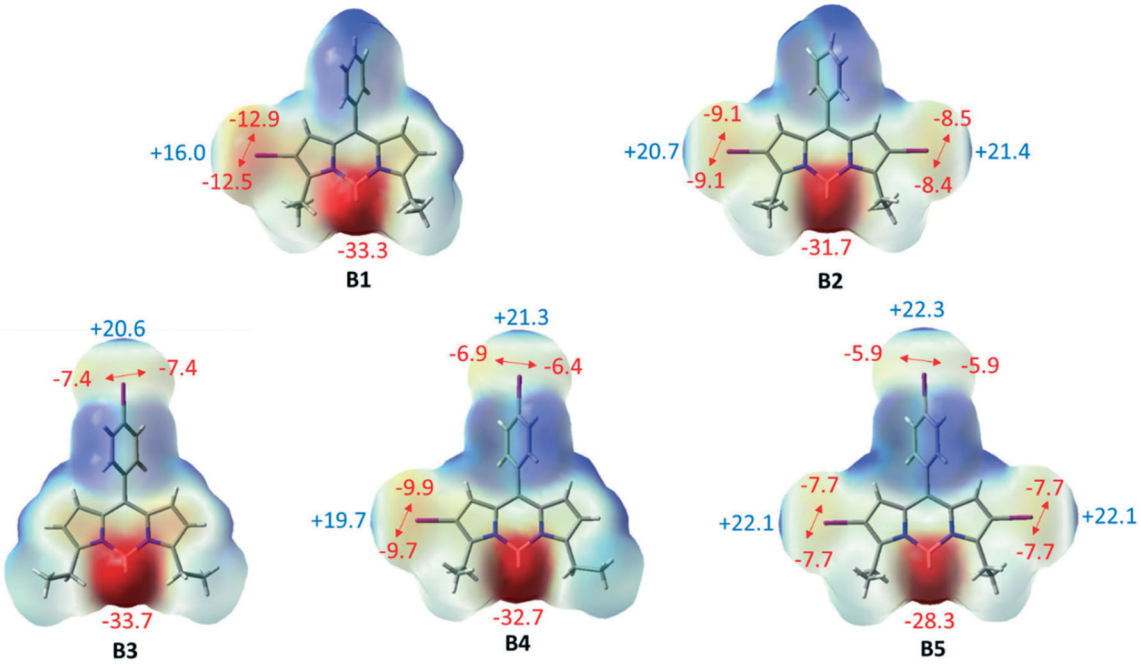

Fig. 8 Electrostatic potential maps of **B1**–**B5** along with the corresponding electrostatic potential values (kcal mol^{-1}).

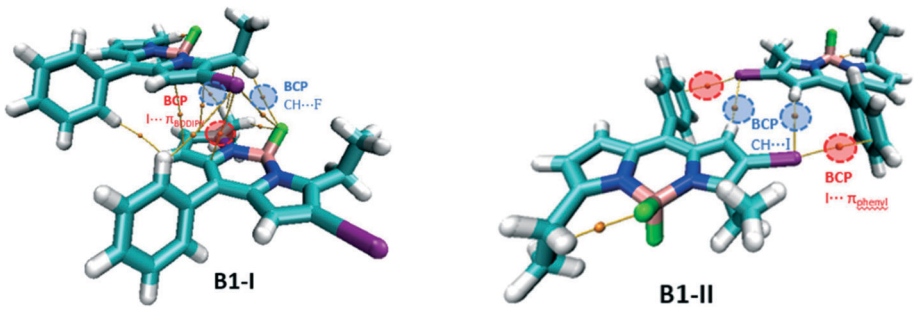

Fig. 9 Molecular graph of the **B1** dimers.

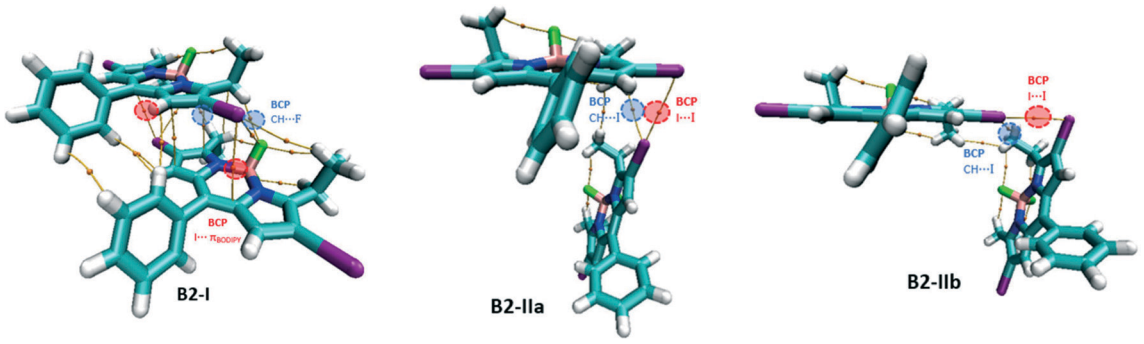

Fig. 10 Molecular graph of the **B2** dimers.

For the **B2** network, three types of dimers, **B2-I**, **B2-IIa** and **B2-IIb**, have been studied (Fig. 10). **B2-I** is the constituent unit of the domino-like arrangement like **B1-I** and possess similar I···π_{BODIPY} and CH···F BCPs. **B2-IIa** and **B2-IIb** represent the unit of the herringbone pattern with different I···I contacts ($d_{I1\cdots I2}$ = 3.976 Å and 4.043 Å, in **B2-IIa** and **B2-IIb** respectively). In **B2-IIa** and **B2-IIb**, there are bond paths connecting two iodine atoms confirming the presence of I···I XB interaction and there is also a BCP in each structure associated with a CH···I hydrogen bonding interaction.

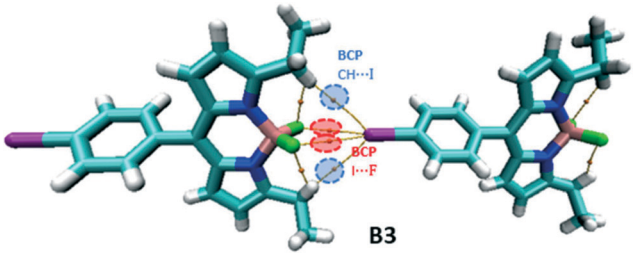

Fig. 11 Molecular graph of the **B3** dimer.

In the **B3** dimer, there are two symmetrical I···F and CH···I BCPs associated with XB and hydrogen bonding interactions, respectively, leading to the formation of the 1D chain structure (Fig. 11).

For the network of **B4**, two dimers, **B4-I** and **B4-II**, are considered, the latter representing the formation of the helical structure and the former, the 2D layers (Fig. 12). **B4-I** possesses similar I···F and CH···I BCPs like **B3**; however, they are not symmetrically bifurcated as this was the case in **B3**. **B4-II**, on the other hand, possesses an I···I BCP associated with a type II XB interaction. Iodine is also involved in the formation of hydrogen bonding interactions, evident from the bond path between iodine and phenyl hydrogen.

For the **B5** network, two different dimers are considered, **B5-I** for the unit of 1D linear chain and **B5-II** for the 3D framework (Fig. 13). Like **B3**, **B5-I** possesses symmetrical bifurcated I···I contacts evident with the BCPs in the molecular graph. There are also CH···I BCPs associated with hydrogen bonding interactions. **B5-II** is similar to **B4-II** with I···I BCPs corresponding to type II XB interactions.

Furthermore, to gain insight into the nature of non-covalent interactions of the studied dimers, the decomposition of the interaction energies (E_{int}) was calculated by the SAPT procedure and shown in Fig. 14. The calculated attractive components E_{elst}, E_{ind} and E_{disp} for all dimers provide sufficient stabilization to overcome the repulsive exchange component, and therefore the resultant E_{int} values are negative (Table S7,† Fig. 14).

The interaction values lie in the range of −4.9 and −3.6 kcal mol^{-1} for the dimers induced by I···I or I···F XB interactions in **B2-IIa/b** and **B3–B5** (Table S7†). For the dimers with I···$\pi_{BODIPY/phenyl}$ interactions (**B1-I**, **B1-II** and **B2-I**) these values are much higher and lie in the range of −10.7 and −20.8 kcal mol^{-1}. Dispersion interactions are highly dominant in these dimers, especially for **B1-I** and **B2-I**, and this is confirmed with the large number of BCPs related to the noncovalent intermolecular interactions. The

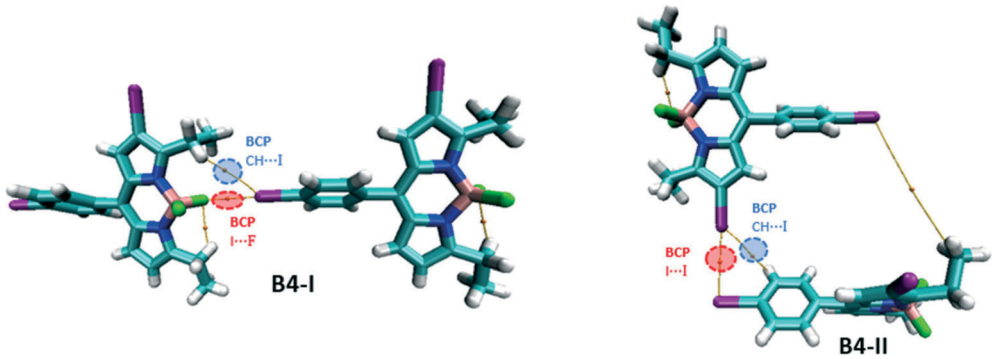

Fig. 12 Molecular graph of the **B4** dimers.

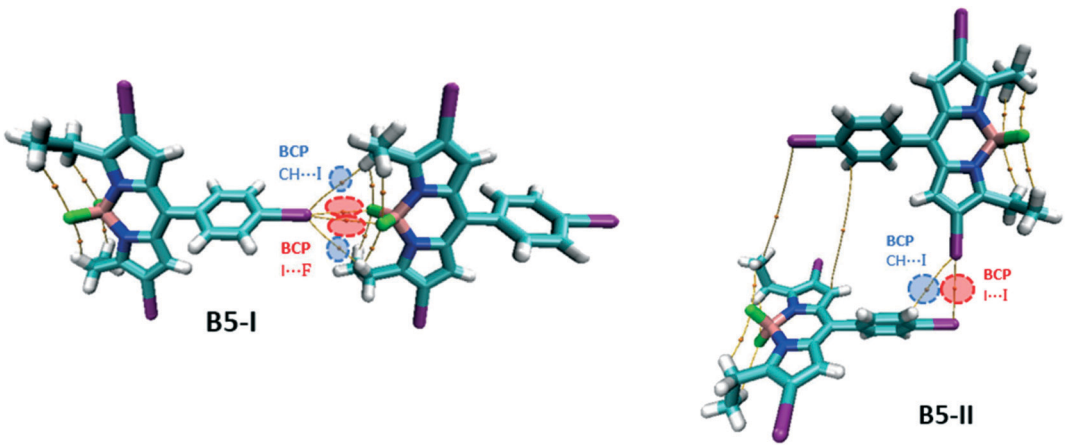

Fig. 13 Molecular graph of the **B5** dimers.

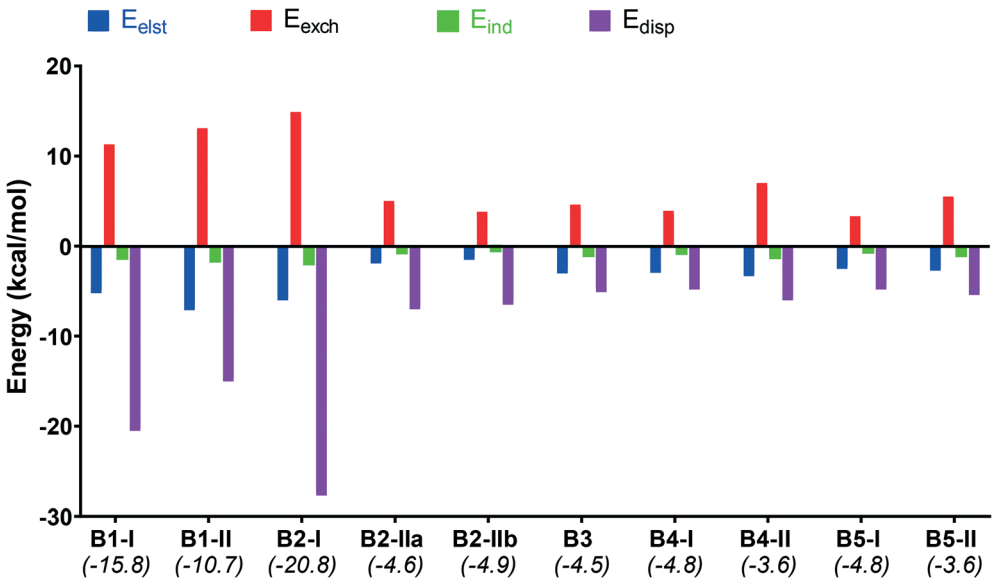

Fig. 14 Summary of SAPT results of the **B1**–**B5** dimers.

electrostatic interactions make the second highest contribution to the interaction energy which suggests that these dimers are jointly stabilized by electrostatic and dispersion interactions.

Conclusion

In this study, we presented the formation of a series of halogen-bonded supramolecular assemblies of iodo-substituted BODIPYs, including tubular-like (**B1**), domino-like (**B2**), 1D linear chain (**B3**), helical (**B4**), and 1D linear chain (**B5**) assemblies by XB (**I**⋯**I**, **I**⋯**F**) and **I**⋯$\boldsymbol{\pi}$ interactions. The formation of halogen bonds in the building blocks of **B1**–**B5** depends on the position and number of iodo substituents on the BODIPY scaffolds. The incorporation of iodine atoms to the 2- and 6-positions (periphery) of BODIPY (**B1**, **B2**) leads to **I**⋯$\boldsymbol{\pi}$ and **I**⋯**I** interactions whereas an iodine atom on the *meso*-phenyl group of BODIPY (**B3**, **B4**, **B5**) leads to **I**⋯**F** and **I**⋯**I** interactions. The molecular electrostatic potential (MEP) showed that the positive potential of σ-holes on the outer tip of the iodine increases with each additional iodo substitution on the periphery of the BODIPY scaffold, whereas iodo on the *meso*-phenyl group of BODIPY has only a small effect. However, the iodine on the phenyl group seems to be able to form more XBs, probably due to its geometric freedom. The SAPT results show that the dispersion and electrostatic components are the major source for all XB formations. These results indicate that halogen⋯halogen interactions can be a useful and efficient tool to adjust the supramolecular self-assembly of BODIPY networks. Therefore, we believe that this systematic study to obtain adjustable self-assemblies of BODIPY frameworks will prove to be of key importance for the future rational design of complex organic electronic materials.

Author contributions

The manuscript was written through contributions of all the authors. All the authors have given approval to the final version of the manuscript.

Conflicts of interest

The authors declare no competing financial interest.

References

1 J. Cao, X. Yan, W. He, X. Li, Z. Li, Y. Mo, M. Liu and Y. B. Jiang, *J. Am. Chem. Soc.*, 2017, **139**, 6605–6610.
2 J. Dahlke, R. Tepper, R. Geitner, S. Zechel, J. Vitz, R. Kampes, J. Popp, M. D. Hager and U. S. Schubert, *Polym. Chem.*, 2018, **9**, 2193–2197.
3 M. Saccone, G. Cavallo, P. Metrangolo, G. Resnati and A. Priimagi, *Top. Curr. Chem.*, 2014, **359**, 147–166.
4 P. Auffinger, F. A. Hays, E. Westhof and P. S. Ho, *Proc. Natl. Acad. Sci. U. S. A.*, 2004, **101**, 16789–16794.
5 L. C. Gilday, S. W. Robinson, T. A. Barendt, M. J. Langton, B. R. Mullaney and P. D. Beer, *Chem. Rev.*, 2015, **115**, 7118–7195.
6 F. Yu, X. Zhang, H. Zhao, Z. Jiang, T. Wang, N. Wang, X. Huang, L. Zhou and H. Hao, *CrystEngComm*, 2022, 3537–3545.
7 C. J. Brown, F. D. Toste, R. G. Bergman and K. N. Raymond, *Chem. Rev.*, 2015, **115**, 3012–3035.
8 M. Raynal, P. Ballester, A. Vidal-Ferran and P. W. N. M. Van Leeuwen, *Chem. Soc. Rev.*, 2014, **43**, 1660–1733.
9 J. Meeuwissen and J. N. H. Reek, *Nat. Chem.*, 2010, **2**, 615–621.
10 S. Portela and I. Fernández, *Eur. J. Org. Chem.*, 2021, **2021**, 6102–6110.
11 X. Zhou, W. Tang, P. Bi, L. Yan, X. Wang, W. K. Wong, X. Hao, B. S. Ong and X. Zhu, *J. Mater. Chem. A*, 2018, **6**, 14675–14680.

12 Y. Liu, C. Zhang, D. Hao, Z. Zhang, L. Wu, M. Li, S. Feng, X. Xu, F. Liu, X. Chen and Z. Bo, *Chem. Mater.*, 2018, **30**, 4307–4312.
13 P. Metrangolo, L. Canil, A. Abate, G. Terraneo and G. Cavallo, *Angew. Chem., Int. Ed.*, 2022, **61**, e202114793.
14 G. R. Desiraju, *J. Am. Chem. Soc.*, 2013, **135**, 9952–9967.
15 I. Benito, R. M. Gomila and A. Frontera, *CrystEngComm*, 2022, **24**, 4440–4446.
16 S. Lim, Y. Kuang and H. A. M. Ardoña, *Front. Chem.*, 2021, **9**, 1–21.
17 T. L. Mako, J. M. Racicot and M. Levine, *Chem. Rev.*, 2019, **119**, 322–477.
18 S. Hou and P. X. Ma, *Chem. Mater.*, 2015, **27**, 7627–7635.
19 Y. Takashima, K. Yonekura, K. Koyanagi, K. Iwaso, M. Nakahata, H. Yamaguchi and A. Harada, *Macromolecules*, 2017, **50**, 4144–4150.
20 W. Dai, X. Niu, X. Wu, Y. Ren, Y. Zhang, G. Li, H. Su, Y. Lei, J. Xiao, J. Shi, B. Tong, Z. Cai and Y. Dong, *Angew. Chem., Int. Ed.*, 2022, **61**, e202200236.
21 J. C. Christopherson, F. Topić, C. J. Barrett and T. Friščić, *Cryst. Growth Des.*, 2018, **18**, 1245–1259.
22 T. H. Borchers, F. Topic, C. Christopherson, O. S. Bushuyev, J. Vainsukas, H. M. Titi, T. Friscic and C. J. Barrett, *Nat. Chem.*, 2022, **14**, 574–581.
23 A. Nitti, C. Botta, A. Forni, E. Cariati, E. Lucenti and D. Pasini, *CrystEngComm*, 2020, **22**, 7782–7785.
24 P. M. J. Szell, S. Zablotny and D. L. Bryce, *Nat. Commun.*, 2019, **10**, 1–8.
25 Ö. D. Ateş, Y. Zorlu, S. D. Kanmazalp, Y. Chumakov, A. G. Gürek and M. M. Ayhan, *CrystEngComm*, 2018, **20**, 3858–3867.
26 F. Heinen, E. Engelage, A. Dreger, R. Weiss and S. M. Huber, *Angew. Chem., Int. Ed.*, 2018, **57**, 3830–3833.
27 A. Dreger, P. Wonner, E. Engelage, S. M. Walter, R. Stoll and S. M. Huber, *Chem. Commun.*, 2019, **55**, 8262–8265.
28 L. E. Bickerton, A. J. Sterling, P. D. Beer, F. Duarte and M. J. Langton, *Chem. Sci.*, 2020, **11**, 4722–4729.
29 F. Heinen, D. L. Reinhard, E. Engelage and S. M. Huber, *Angew. Chem.*, 2021, **60**, 5069–5073.
30 R. L. Sutar and S. M. Huber, *ACS Catal.*, 2019, **9**, 9622–9639.
31 R. Gutzler, C. Fu, A. Dadvand, Y. Hua, J. M. MacLeod, F. Rosei and D. F. Perepichka, *Nanoscale*, 2012, **4**, 5965–5971.
32 N. B. Topic, N. Bedeković, V. Stilinovic and D. Cinčić, *Cryst. Growth Des.*, 2022, **22**, 3981–3989.
33 F. F. Awwadi, R. D. Willett, K. A. Peterson and B. Twamley, *Chem. – Eur. J.*, 2006, **12**, 8952–8960.
34 S. Scheiner, *Cryst. Growth Des.*, 2022, **22**, 2692–2702.
35 A. Varadwaj, H. M. Marques and P. R. Varadwaj, *Molecules*, 2019, **24**, 379.
36 M. A. A. Ibrahim and N. A. M. Moussa, *ACS Omega*, 2020, **5**, 21824–21835.
37 P. R. Varadwaj, A. Varadwaj and H. M. Marques, *Inorganics*, 2019, **7**, 11–17.
38 M. A. Niyas, R. Ramakrishnan, V. Vijay, E. Sebastian and M. Hariharan, *J. Am. Chem. Soc.*, 2019, **141**, 4536–4540.
39 T. S. Spilfogel, H. M. Titi and T. Friščić, *Cryst. Growth Des.*, 2021, **21**, 1810–1832.
40 M. Yamada, R. Kanazawa and F. Hamada, *CrystEngComm*, 2014, **16**, 2605–2614.
41 M. E. Brezgunova, E. Aubert, S. Dahaoui, P. Fertey, S. Lebègue, C. Jelsch, J. G. Ángyán and E. Espinosa, *Cryst. Growth Des.*, 2012, **12**, 5373–5386.
42 J. Teyssandier, K. S. Mali and S. De Feyter, *ChemistryOpen*, 2020, **9**, 225–241.
43 H. Li, M. Telychko, L. Zhou, Z. Chen, X. Peng, W. Ji, J. Lu and K. P. Loh, *J. Phys. Chem. C*, 2022, **126**, 4241–4247.
44 S. An, A. Hao and P. Xing, *ACS Nano*, 2021, **15**, 15306–15315.
45 D. Aydin Tekdaş, G. Viswanathan, S. Z. Topal, C. Y. Looi, W. F. Wong, G. M. Y. Tan, Y. Zorlu, A. G. Gürek, H. B. Lee and F. Dumoulin, *Org. Biomol. Chem.*, 2016, **14**, 2665–2670.
46 M. Ozdemir, D. Choi, G. Kwon, Y. Zorlu, B. Cosut, H. Kim, A. Facchetti, C. Kim and H. Usta, *ACS Appl. Mater. Interfaces*, 2016, **8**, 14077–14087.
47 J. Zhou, Y. Zhang, G. Yu, M. R. Crawley, C. R. P. Fulong, A. E. Friedman, S. Sengupta, J. Sun, Q. Li, F. Huang and T. R. Cook, *J. Am. Chem. Soc.*, 2018, **140**, 7730–7736.
48 A. Nagai, K. Kokado, J. Miyake and Y. Chujo, *Polym. J.*, 2010, **42**, 37–42.
49 G. Das, S. Cherumukkil, A. Padmakumar, V. B. Banakar, V. K. Praveen and A. Ajayaghosh, *Angew. Chem.*, 2021, **201002**, 7851–7859.
50 S. P. Singh and T. Gayathri, *Eur. J. Org. Chem.*, 2014, **2014**, 4689–4707.
51 H. Klfout, A. Stewart, M. Elkhalifa and H. He, *ACS Appl. Mater. Interfaces*, 2017, **9**, 39873–39889.
52 M. Ozdemir, D. Choi, Y. Zorlu, B. Cosut, H. Kim, C. Kim and H. Usta, *New J. Chem.*, 2017, **41**, 6232–6240.
53 D. A. Merkushev, S. D. Usoltsev, Y. S. Marfin, A. P. Pushkarev, D. Volyniuk, J. V. Grazulevicius and E. V. Rumyantsev, *Mater. Chem. Phys.*, 2017, **187**, 104–111.
54 M. M. Ayhan, E. Özcan, F. Alkan, M. Çetin, İ. Ün, D. Bardelang and B. Çoşut, *Mater. Adv.*, 2022, **3**, 547–553.
55 H. Wang, W. Zhao, X. Liu, S. Wang and Y. Wang, *ACS Appl. Bio Mater.*, 2020, **3**, 593–601.
56 T. Kowada, H. Maeda and K. Kikuchi, *Chem. Soc. Rev.*, 2015, **44**, 4953–4972.
57 W. H. Garciá-Santos, J. Ordóñez-Hernández, M. Farfán-Paredes, H. M. Castro-Cruz, N. A. Maciás-Ruvalcaba, N. Farfán and A. Cordero-Vargas, *J. Org. Chem.*, 2021, **86**, 16315–16326.
58 P. De Bonfils, L. Péault, P. Nun and V. Coeffard, *Eur. J. Org. Chem.*, 2021, **2021**, 1809–1824.
59 J. Zou, Z. Yin, K. Ding, Q. Tang, J. Li, W. Si, J. Shao, Q. Zhang, W. Huang and X. Dong, *ACS Appl. Mater. Interfaces*, 2017, **9**, 32475–32481.
60 S. A. Sharber, W. J. Mullin and S. W. Thomas, *Chem. Mater.*, 2021, **33**, 6640–6661.
61 Y. Lee, R. M. Malamakal, D. M. Chenoweth and J. M. Anna, *J. Phys. Chem. Lett.*, 2020, **11**, 877–884.
62 M. Su, Q. Han, X. Yan, Y. Liu, P. Luo, W. Zhai, Q. Zhang, L. Li and C. Li, *ACS Nano*, 2021, **15**, 5032–5042.

63 X. Yan, M. Su, Y. Liu, Y. Zhang, H. Zhang and C. Li, *Adv. Funct. Mater.*, 2021, **31**, 1–11.
64 E. Özcan, B. Dedeoglu, Y. Chumakov, A. G. Gürek, Y. Zorlu, B. Coşut and M. M. Ayhan, *Chem. – Eur. J.*, 2021, **27**, 1603–1608.
65 M. M. Ayhan, E. Özcan, B. Dedeoglu, Y. Chumakov, Y. Zorlu and B. Coşut, *CrystEngComm*, 2021, **23**, 268–272.
66 E. Özcan, B. Dedeoglu, Y. Chumakov, Y. Zorlu, B. Çoşut and M. M. Ayhan, *CrystEngComm*, 2021, **23**, 6365–6375.
67 B. Matarranz and G. Fernández, *Chem. Phys. Rev.*, 2021, **2**, 041304.
68 *APEX2. Ver. 2014.11–0*, Bruker, 2014.
69 *W. SAINT, version 8.34A, Bruker*, Bruker AXS Inc., Madison, 2013.
70 *W. SADABS, version2014/5, Bruker*, Bruker AXS Inc., Madison, 2014.
71 G. M. Sheldrick, *Acta Crystallogr., Sect. C: Struct. Chem.*, 2015, **71**, 3–8.
72 O. V. Dolomanov, L. J. Bourhis, R. J. Gildea, J. A. K. Howard and H. Puschmann, *J. Appl. Crystallogr.*, 2009, **42**, 339–341.
73 A. L. Spek, *Acta Crystallogr., Sect. D: Biol. Crystallogr.*, 2009, **65**, 148–155.
74 C. F. Macrae, P. R. Edgington, P. McCabe, E. Pidcock, G. P. Shields, R. Taylor, M. Towler and J. Van De Streek, *J. Appl. Crystallogr.*, 2006, **39**, 453–457.
75 M. J. Frisch, G. W. Trucks, H. B. Schlegel, G. E. Scuseria, M. A. Robb, J. R. Cheeseman, G. Scalmani, V. Barone, G. A. Petersson, H. Nakatsuji, X. Li, M. Caricato, A. Marenich, J. Bloino, B. G. Janesko, R. Gomperts, B. Mennucci, H. P. Hratchian, J. V. Ortiz, A. F. Izmaylov, J. L. Sonnenberg, D. Williams-Young, F. Ding, F. Lipparini, F. Egidi, J. Goings, B. Peng, A. Petrone, T. Henderson, D. Ranasinghe, V. G. Zakrzewski, J. Gao, N. Rega, G. Zheng, W. Liang, M. Hada, M. Ehara, K. Toyota, R. Fukuda, J. Hasegawa, M. Ishida, T. Nakajima, Y. Honda, O. Kitao, H. Nakai, T. Vreven, K. Throssell, J. A. Montgomery, Jr., J. E. Peralta, F. Ogliaro, M. Bearpark, J. J. Heyd, E. Brothers, K. N. Kudin, V. N. Staroverov, T. Keith, R. Kobayashi, J. Normand, K. Raghavachari, A. Rendell, J. C. Burant, S. S. Iyengar, J. Tomasi, M. Cossi, J. M. Millam, M. Klene, C. Adamo, R. Cammi, J. W. Ochterski, R. L. Martin, K. Morokuma, O. Farkas, J. B. Foresman and D. J. Fox, *Gaussian 16, Revision C.01*, Gaussian, Inc., Wallingford CT, 2016.
76 T. Lu and F. Chen, *J. Comput. Chem.*, 2012, **33**, 580–592.
77 B. Jeziorski, R. Moszynski and K. Szalewicz, *Chem. Rev.*, 1994, **94**, 1887–1930.
78 T. Korona, R. Moszynski and B. Jeziorski, *J. Chem. Phys.*, 1996, **105**, 8178–8186.
79 K. Szalewicz, *Wiley Interdiscip. Rev.: Comput. Mol. Sci.*, 2012, **2**, 254–272.
80 J. M. Turney, A. C. Simmonett, R. M. Parrish, E. G. Hohenstein, F. A. Evangelista, J. T. Fermann, B. J. Mintz, L. A. Burns, J. J. Wilke, M. L. Abrams, N. J. Russ, M. L. Leininger, C. L. Janssen, E. T. Seidl, W. D. Allen, H. F. Schaefer, R. A. King, E. F. Valeev, C. D. Sherrill and T. D. Crawford, *Wiley Interdiscip. Rev.: Comput. Mol. Sci.*, 2012, **2**, 556–565.
81 M. Gorbe, A. M. Costero, F. Sancenón, R. Martínez-Máñez, R. Ballesteros-Cillero, L. E. Ochando, K. Chulvi, R. Gotor and S. Gil, *Dyes Pigm.*, 2019, **160**, 198–207.
82 B. C. De Simone, G. Mazzone, J. Pirillo, N. Russo and E. Sicilia, *Phys. Chem. Chem. Phys.*, 2017, **19**, 2530–2536.
83 V. Mani, V. G. Krishnakumar, S. Gupta, S. Mori and I. Gupta, *Sens. Actuators, B*, 2017, **244**, 673–683.
84 Y. Chen, L. Wan, D. Zhang, Y. Bian and J. Jiang, *Photochem. Photobiol. Sci.*, 2011, **10**, 1030–1038.
85 R. Hu, E. Lager, A. Aguilar-Aguilar, J. Liu, J. W. Y. Lam, H. H. Y. Sung, I. D. Williams, Y. Zhong, K. S. Wong, E. Peña-Cabrera and B. Z. Tang, *J. Phys. Chem. C*, 2009, **113**, 15845–15853.